Investigation of basic processes in a lithium Lorentz force accelerator through plasma flow simulation

K. Sankaran* and E. Y. Choueiri†
Electric Propulsion & Plasma Dynamics Laboratory, Princeton University, Princeton, NJ 08544

S. C. Jardin‡
Princeton Plasma Physics Laboratory, Princeton University, Princeton, NJ 08544

The flowfield of the lithium Lorentz force accelerator (LiLFA), a promising high-power plasma thruster for spacecraft propulsion, was simulated numerically using an advanced plasma-fluid code specifically developed for this purpose, in order to obtain insight into underlying physical processes that had been poorly understood. The parallelized axisymmetric code features detailed physical models and proven MHD solution schemes. The flowfields of plasma density, velocity, ionization, and anomalous resistivity are shown to change qualitatively with the total current, and illustarte how increasing the current leads to a stronger plasma pinching by radial Lorentz forces, an increase in anomalous resitivity and a decrease in the gasdyanmic contribution to thrust. The breakdown and scaling of the various components of thrust and power are revealed. The motion of the $\beta = 1$ line with increasing current was shown to provide an illustration of the anode starvation mechanism that leads to the current conduction crisis called "onset".

*Presently Assistant Professor, Physics Department, Whitworth College, WA.
†Chief Scientist at the Electric Propulsion & Plasma Dynamics Laboratory. Associate Professor, MAE Dept.
‡Principal Research Scientist, Princeton Plasma Physics Lab; Lecturer with the rank of Professor, Astrophysical Sciences Dept.

Nomenclature

$\mathbf{B}$	Magnetic induction
$\bar{\bar{\mathcal{B}}}_M$	Maxwell stress tensor
e	Charge of an electron
E	Electric field strength
E'	Electric field seen by the plasma
$\mathcal{E}$	Energy density of the plasma
h	Planck's constant
g	Statistical weight of an energy level
I_{sp}	Specific impulse
$\bar{\bar{\mathcal{I}}}$	Identity matrix
$\mathbf{j}$	Current per unit area
J	Current
k_B	Boltzmann's constant
k	Coefficient thermal conduction
m	Mass of a particle
n	Number density of a species
p	Pressure
$\mathbf{q}$	Energy flux
Q	Collision cross section
Q	Partition function
T	Temperature
T	Thrust
$\mathbf{u}$	Fluid velocity
Z	Effective ionization level = n_e/n
ϵ	Electronic energy level
ϵ_o	Permittivity of free space
η	Resistivity
μ_o	Permeability of free space
ν	Collision frequency
ξ	Dimensionless current
ρ	Mass density
ψ	Stream function = rB_θ
Ω	Hall parameter
Subscripts	
an	Anomalous
cl	Classical
e	Electrons
el	Electronic
ex	Exhaust
EM	Electromagnetic
h	Heavy species (Ar I, Ar II, Ar III, Ar IV)
i	Ions
mfp	Mean free path
th	Thermal
tr	Translation
w	Wall

I. INTRODUCTION

The lithium Lorentz force accelerator (LiLFA) is a plasma thruster[1–5] that uses the Lorentz force, produced by the interaction of current with self-induced magnetic fields, to accelerate lithium propellant (with barium additive), fed through multi-channel hollow cathodes, to high velocities ($10^4 - 10^5$ m/s) of interest to spacecraft propulsion. In particular, high-energy missions such as robotic and piloted exploration of the moon, mars and the outer planets, had been shown[6–8] to potentially benefit from the high specific impulse of the LiLFA and its ability to efficiently process many hundreds of kilowatts of power from a nuclear power plant in a simple compact device. Due to the LiLFA's promise, sustained efforts are being made in the US and Russia[1–5] to study it and improve its performance and lifetime.

While the work of Ageyev *et al.* [1] has demonstrated efficiency of 60% and I_{sp} of 4000 s, with 500 hours of erosion free operation at power levels up to 500 kW, there are no published records of systematic experimental or theoretical investigations of the underlying physical processes. Though the reported data (terminal characteristics (I_{sp}, and η) at the highest operating condition (J = 8.0 to 10.0 kA, $\dot{m}$ = 0.2 to 0.3 g/s)) are good for bolstering the technology readiness level of this device, lack of information on interior properties limits their utility for understanding plasma processes in the device. For this purpose, we used the code we described in refs.[9–12] to simulate the flowfield of the LiLFA. Since there are presently no experimental data for the LiLFA internal flowfields, the goal here is not comparison with experiments (this code has already been validated in detail for the self-field magnetoplasmadynamic thruster (MPDT) called the full-scale benchmark thruster (FSBT)[12]), but rather gain insight into some of the internal processes in the LiLFA. Moreover, the difficulty of obtaining measurements inside the thruster chamber, where the harsh environment of a high current (1-10 kA) discharge and condensing lithium render probing extremely difficult, further gives a motivation for relying on realistic numerical simulations to understand the internal processes.

In §II, we describe the governing equations and the physical models used in this simulation. In §III we briefly discuss the discretization method and the boundary conditions imposed on the solver to calculate the flowfield in self-field plasma thrusters. In §IV we present the results from the simulation of plasma flows in the LiLFA. In §V we use these results to investigate some underlying physical processes in the LiLFA.

II. PHYSICAL MODEL

While we have already described the physical model in refs.[11, 12], we will give here only the details relevant to the present discussion.

For typical operating conditions of interest to high-power (> 100 kW) plasma thrusters, the electron and ion densities are $\mathcal{O}\left(10^{21}\right)/\mathrm{m}^3$, mass-averaged velocities are $\mathcal{O}(10^4)$ m/s, temperatures are $\sim$ 2 eV, thermodynamic pressures are $\mathcal{O}(10^{-1} - 1)$ Torr, and magnetic pressures are $\mathcal{O}(1 - 10)$ Torr. The LiLFA plasma in this regime can be treated as quasineutral because the dimensions of the device are much larger than the Debye length, $L/\lambda_D \sim \mathcal{O}\left(10^5\right)$, the residence time scale is much larger than the time scale needed for the electrons to adjust to the charge separation, $\tau_{res}\,\omega_{pe} \sim \mathcal{O}\left(10^5\right)$, and inertial forces are far greater than the electrostatic force due to charge separation, $\rho\mathbf{U}\cdot\nabla\mathbf{U}/\rho_e E \sim \mathcal{O}\left(10^9\right)$. Moreover, a continuum MHD treatment is reasonable because the characteristic length scale of the device is found to be much larger than the mean free path between collisions, $L/\lambda_{mfp} \sim \mathcal{O}\left(10^3\right)$.

The governing equations for this MHD flow problem are the conservation relations for mass, momentum, magnetic flux, and energy. The conservation relations for mass *density*, momentum *density*, magnetic flux, and energy *density* can be written in the form[11]:

$$\frac{\partial}{\partial t}\begin{bmatrix}\rho\\ \rho\mathbf{u}\\ \mathbf{B}\\ \mathcal{E}\end{bmatrix}+\nabla\cdot\begin{bmatrix}\rho\mathbf{u}\\ \rho\mathbf{u}\mathbf{u}+\bar{\bar{p}}-\bar{\bar{\mathcal{B}}}_M\\ \mathbf{u}\mathbf{B}-\mathbf{B}\mathbf{u}\\ (\mathcal{E}+p)\,\mathbf{u}-\bar{\bar{\mathcal{B}}}_M\cdot\mathbf{u}\end{bmatrix}=\mathbf{D}. \tag{1}$$

The right hand side of the equation, $\mathbf{D}$, contains the dissipative effects that are physical in nature,

$$\mathbf{D}=\begin{bmatrix}0\\ 0\\ -\nabla\times\left(\eta\mathbf{j}+\frac{\mathbf{j}\times\mathbf{B}}{en_e}\right)\\ \nabla\cdot\left[\frac{-\mathbf{E}'\times\mathbf{B}}{\mu_o}+k_{th}\nabla T\right]\end{bmatrix}, \tag{2}$$

and they too are written as divergence of fluxes, as described in ref.[12].

In the momentum equation, $\bar{\bar{\mathcal{B}}}_M = \frac{1}{\mu_o}\left[\mathbf{BB} - \frac{B^2}{2}\bar{\bar{\mathcal{I}}}\right]$ is the magnetic part of the Maxwell stress tensor, and it satisfies the relation,

$$\nabla \cdot \bar{\bar{\mathcal{B}}}_M = \mathbf{j} \times \mathbf{B} \ . \tag{3}$$

In Faraday's law, the contribution of back EMF to the change in magnetic field is written as a divergence of a flux,

$$-\nabla \times (\mathbf{u} \times \mathbf{B}) = \nabla \cdot (\mathbf{uB} - \mathbf{Bu}) \ . \tag{4}$$

The energy equation is written in terms of the energy density (energy per unit volume), $\mathcal{E}$, which includes the internal energy, kinetic energy and the magnetic field energy. The dissipative flux of energy, $\nabla \cdot \mathbf{q}$, contains an Ohmic heating term (written in terms of divergence of the Poynting flux), and thermal conduction,

$$\nabla \cdot \mathbf{q} = \nabla \cdot \left[\frac{\mathbf{B} \times \mathbf{E}'}{\mu_0} + k\nabla T\right] \ .$$

In addition to the total energy equation, we need to account for the disparity between electron and ion temperatures. The conservation relations for the internal energy density of electrons, $\mathcal{E}_e$, can be written as

$$\frac{\partial \mathcal{E}_e}{\partial t} + \nabla \cdot [\mathcal{E}_e \mathbf{u}] + p_e \nabla \cdot \mathbf{u} = \eta j^2 - \Delta\dot{\mathcal{E}}_{ie} + \nabla \cdot (k_e \nabla T_e) \ . \tag{5}$$

In the above expression, ηj^2 is the Ohmic heating term. The rate of exchange of energy per unit volume between the electrons and the ions, through collisions, $\Delta\dot{\mathcal{E}}_{ie}$, is

$$\Delta\dot{\mathcal{E}}_{ie} = \frac{3\rho_e \nu_{ei}}{M_i} k_B \left(T_e - T_i\right) \ , \tag{6}$$

where ρ_e is the electron mass density, and ν_{ei} is the average collision frequency between electrons and ions. The internal energy of ions can be obtained by subtracting electron internal energy from the total internal energy.

A. Transport Phenomena

The transport phenomena included in our model are electron and ion thermal conduction, classical electrical resistivity with Hall effect, and anomalous transport[13].

The anomalous transport model takes into account the enhanced transport due to momentum exchange between particles in the plasma and waves induced by current-driven microinstabilities in a collisional and finite-β magnetized plasma[14]. The ratio of the anomalous to classical collision frequencies was obtained from ref.[13] to be,

$$\frac{\nu_{e_{an}}}{\nu_{e_{cl}}} = \left\{0.192 + 3.33 \times 10^{-2}\Omega_e + 0.212\Omega_e^2 - 8.27 \times 10^{-5}\Omega_e^3\right\} + \frac{T_h}{T_e}\left\{1.23 \times 10^{-3} - 1.58 \times 10^{-2}\Omega_e - 7.89 \times 10^{-3}\Omega_e^3\right\} \ . \tag{7}$$

As a result, the effective resistivity of the plasma can be expressed as

$$\eta_{\text{eff}} = \frac{m_e \left(\nu_{e_{cl}} + \nu_{e_{an}}\right)}{e^2 n_e} \ , \tag{8}$$

and ref.[15] shows how this is incorporated into this code.

B. Equation of State

For lithium, the ideal gas model is not accurate for temperatures (1 - 5 eV) of interest to propulsion. As energy is deposited into internal modes, the ratio of specific heats deviates significantly from the ideal value of 5/3. In our model, the ratio of specific heats, shown in Fig.1, was computed from first principles using the partition function, and electronic energy levels for lithium, obtained from refs.[16, 17], are shown in Table I. Using these, the electronic energy partition function can be calculated as,

$$Q_{el} = \sum_i g_i \; e^{-\epsilon_i / k_B T_e}. \tag{9}$$

Then, the total partition function is

$$Q_{\text{tot}} = Q_{tr} Q_{el}. \tag{10}$$

With this, the internal energy per unit volume, $\mathcal{E}$, can be computed,

$$\mathcal{E} = n k_B T^2 \frac{\partial \ln Q_{\text{tot}}}{\partial T}. \tag{11}$$

The definition of specific enthalpy,

$$h \equiv \mathcal{E} + p, \tag{12}$$

can then be used to calculate the specific heat at constant pressure,

$$c_p \equiv \left. \frac{\partial h}{\partial T} \right|_p, \tag{13}$$

and the specific heat at constant volume

$$c_v \equiv \left. \frac{\partial \mathcal{E}}{\partial T} \right|_v. \tag{14}$$

Armed with these parameters, the ratio of specific heats can be calculated as,

$$\gamma \equiv \frac{c_p}{c_v}. \tag{15}$$

The resulting ratios of specific heats are shown in Fig.(1). As the temperature increases, progressively more electronic energy levels become accessible, and consequently γ continues to drop. But for lithium, γ quickly reverts to its ideal value of 5/3 because the gap between the first and second ionization potentials (5.39 eV and 75.62 eV) is very large. This fact is significant for propulsive applications as much of the power in the gas-fed MPDT exhaust is in internal modes[18], and is not easily recovered (hence known as "frozen flow"); but for lithium, internal modes do not represent an as significant loss mechanism.

C. Ionization

It is imperative that, within the acceleration region, a significant fraction of the working fluid remains in a state of ionization, as the free charges are responsible for carrying current, and thereby establishing the electromagnetic Lorentz forces required for acceleration[19]. In the present work, we use a multi-level equilibrium ionization model, where the densities of electrons, n_e, ions, n_i, and neutrals, n_o, are related by the Saha equation,

Li I		Li II		Li III	
E_l^0 (eV)	g_l^0	E_l^+ (eV)	g_l^+	E_l^{++} (eV)	g_l^{++}
0.000	2	0.000	1	0.000	2
1.848	6	59.021	3	91.788	8
3.373	2	60.920	1	108.785	18
3.834	6	61.281	9	1114.735	32
3.879	10	62.216	3		
4.341	12	68.780	3		
4.522	6	69.278	1		
4.541	10	69.368	9		
4.541	14	69.584	15		
4.748	2	69.588	5		
4.837	6	69.647	3		
4.847	24				

TABLE I: Energy levels and statistical weights in lithium and lithium ions (obtained from refs.[16, 17])

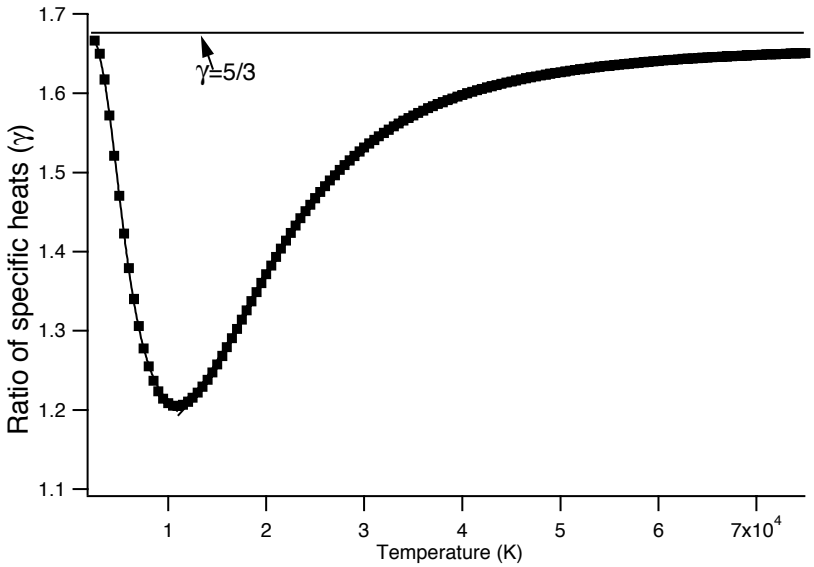

FIG. 1: Variation of the ratio of specific heats for lithium.

$$\frac{n_i n_e}{n_{i-1}} = \frac{2\left(2\pi m_e k_B T_e\right)^{3/2}}{h^3} \frac{\sum_l g_l^i \; e^{-\epsilon_l^i/k_B T_e}}{\sum_l g_l^{i-1} \; e^{-\epsilon_l^{i-1}/k_B T_e}} = K_i, \tag{16}$$

in which ϵ_l^i is the l^{th} energy level of the species of ionization level i, g_l^i is the corresponding statistical weight, and K_i is the equilibrium constant. Lithium's first and second ionization potentials are 5.39 eV and 75.62 eV respectively. The relevant energy levels of the lithium atom, its ions, and their statistical weights, obtained from refs.[16, 17], are given in Table (I), and have to be adjusted to the ionization potentials given above.

For a model with N levels of ionization, the electron number density can be obtained by finding the single positive root of the polynomial[20],

$$n_e^{N+1} + \sum_{l=1}^{N} \left[n_e^{N-l} \left(n_e - l n_o\right) \prod_{m=1}^{l} K_m \right] = 0 \; , \tag{17}$$

where n_o is the total number density of all nuclei, and the equilibrium constant, K_m is from eqn.(16). The resulting ionization fraction, $Z = n_e/n$, is plotted in Fig.(2).

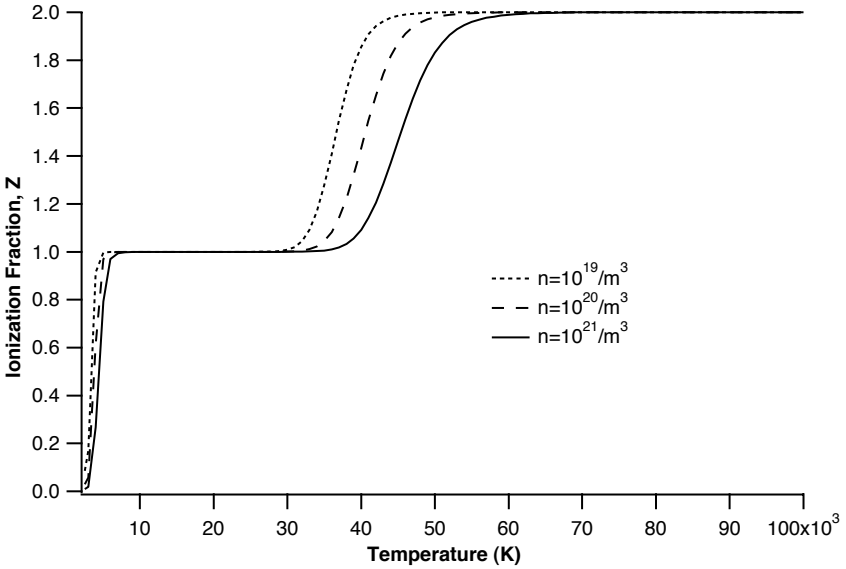

FIG. 2: Variation of ionization fraction with temperature for lithium.

Although the plasma in high-power plasma accelerators is generally in a state of ionizational nonequilibrium [21], the equilibrium model described above has been shown[12] to give results that compare favorably with experimental measurements.

III. NUMERICAL SOLUTION

The techniques for the numerical solution of eqns.(1-5) are described in ref.[11], and in this section we will only discuss how they are used to simulate the flowfield in the LiLFA.

A. Spatial Discretization

Mathematically, the governing equations (eqns.(1-5)) are mixed hyperbolic and parabolic partial differential equations. The discretization scheme for the hyperbolic (convective) part of the problem involves using the characteristics to estimate fluxes through the cell surfaces, and is described in ref.[11]. Unlike convective fluxes, dissipative fluxes depend on gradients, and require computation of derivatives across the surfaces to estimate $j_r, j_z, \partial T/\partial r$, and $\partial T/\partial z$. In an orthogonal grid system, we can estimate gradients by simply differencing the values in adjacent cells. However, in a non-orthogonal grid, the adjacent cells/points are *not* along the lines of constant "r", or "z". Therefore we have to estimate gradients in a different manner. This involves using the Stokes theorem, and this method is described in ref.[12].

B. Boundary Conditions

The computational domain used for the simulation is shown in Fig.(3). The dimensions were obtained from the NASA-JPL version of the LiLFA[22] (shown in Fig.(4)), which itself is based on the configuration of Ageyev *et al.*[1].

We will now discuss the evaluation of fluxes at surfaces #1 to 8 in Fig.(3).

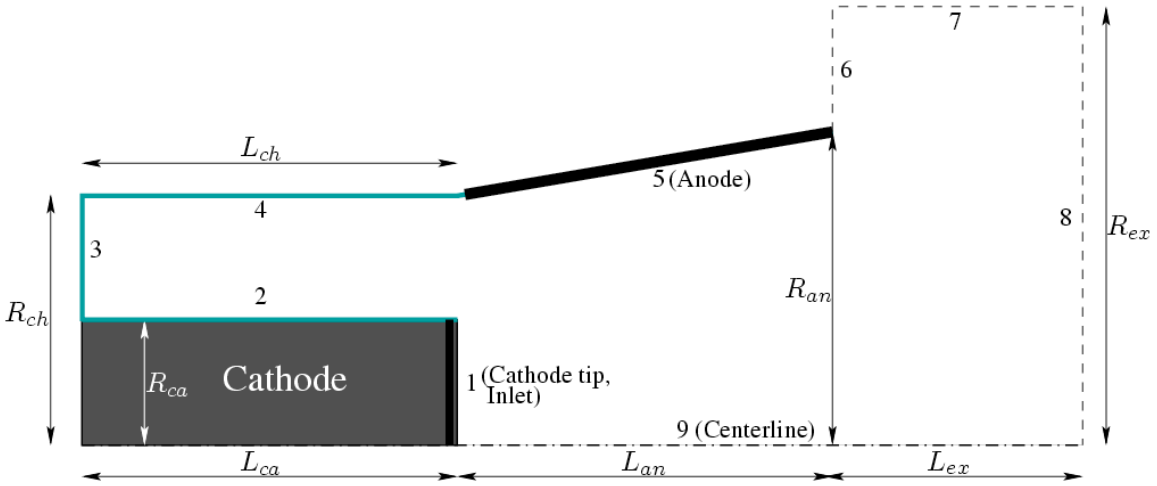

FIG. 3: Computational domain of the Lithium Lorentz Force Accelerator (LiLFA), where R_{ca}= 5.0 cm, R_{ch}= 11.0 cm, R_{an}= 13.4 cm, R_{ex}= 20.0 cm, L_{ca}= 26.0 cm, L_{ch}= 26.0 cm, L_{an}= 26.5 cm, and L_{ex}= 22.5 cm.

C. Flow Properties

Inlet

Unlike gas-fed MPDTs, the propellant enters the LiLFA not through the backplate (surface #3) but through the cathode exit (surface #1 in Fig.(3)). The LiLFA uses a multi-channel hollow cathode[1, 2, 4, 23–25] inside which a stream of neutral lithium vapor is ionized efficiently, and ejected uniformly into the thruster through the cathode exit. Describing the operation of the hollow cathode[26] itself is beyond the scope of this work, which concerns only with what happens to the plasma once it enters the thrust chamber. Therefore, in this code, a specified mass flow rate (typically 0.25 g/s) of the ionized lithium plasma ($Z = 1$) enters at a specified temperature ($T_e = T_h = 0.75$ eV) through surface # 1.

Solid Boundaries

A standard solid-body boundary condition, $\mathbf{n} \cdot \mathbf{u} = 0$, is applied at the cathode outer surface (#2), backplate (#3), chamber inner surface (#4), and the anode nozzle (#5). Note that at the anode, $\mathbf{n}$ and $\mathbf{u}$ have both radial and axial components.

Anode Exit Freestream

After the plasma exits the thruster, it expands downstream as a plume because the exit pressure is greater than the ambient pressure. At the anode exit plane, the plume could expand upstream (through surface #6 in Fig.(3)). The flow through this plane could be either subsonic or supersonic. If the flow is subsonic, one needs to specify pressure, density, or temperature outside of the domain. In this code, an outside temperature of $T_{out} = 300$ K is specified. If the flow through surface #6 is supersonic, information out of the domain cannot affect the solution inside the domain. In that case, velocity and density are set to have zero gradients in the normal direction.

Freestream

At the other freestream boundaries, #7 and #8 in Fig.(3), velocity, density, pressure, temperature, and specific heats are set to have zero gradients in the normal direction.

Centerline

At the axis of symmetry, all convective fluxes and radial gradients are set to zero.

D. Field Properties

The magnetic field is computed from Faraday's law, which through Stokes theorem can be written as,

$$\int_A \frac{\partial \mathbf{B}}{\partial t} \cdot d\mathbf{A} = -\oint_C \mathbf{E} \cdot d\mathbf{l} \ . \tag{18}$$

In the cell-centered scheme used in this work, eqn.(18) implies that the evolution of the magnetic flux is specified by the contour integral of the electric field around a cell. Therefore, the only information required is the electric field along the boundaries.

Inlet

As described earlier, all the propellant enters the thruster through the cathode exit (surface #1 in Fig.(3)). Consequently, all the current attaches there. Faraday's law requires estimation of electric field at this boundary to compute the evolution of magnetic field in the plasma adjacent to this boundary. This can be estimated as,

$$E_r|_{z_{ca}} = E_r|_{z_{ca}+\Delta z} + \Delta z \left(\frac{\mu_o}{2\pi r} \frac{dJ}{dt} - \left(\frac{E_z|_{r+\Delta r} - E_z|_r}{\Delta r} \right) \right), \tag{19}$$

where $E_r|_{z_{ca}+\Delta z}$, $E_z|_{r+\Delta r}$ and $E_z|_r$ are computed self consistently in the plasma adjacent to this boundary.

Cathode Outer Surface

In reality, the outer surface of the cathode (surface #2 in Fig.(3)) is made of a refractory metal (typically tungsten). But because there is little or no propellant upstream of the cathode exit, there is no current attachment on the outer surface of the cathode. So, in this code, this surface is modeled as an insulator to prevent current attachment in the near-vacuum region. Estimation of electric field at an insulating boundary is described in the following part.

Chamber Inner Surface

The thruster designs in ref.[1] and in Fig.(4) have a shield in the inner surface of the chamber (surface #4 in Fig.(3)), and there is no current attachment on it. So, as at the cathode outer surface, there is a need to evaluate the electric field at an insulating surface. Since all the current is downstream of these insulators, the electric field is

$$E_z(R_{ch}, z) = E_z(R_{ch} - \Delta r, z) + \Delta r \left(\frac{1}{r} \frac{\partial \psi}{\partial t} + \frac{\partial E_r}{\partial z} \right). \tag{20}$$

Anode Nozzle

Due to the no mass flux condition, the electric field at the anode is entirely resistive, and is given by,

$$\mathbf{E}_w = \eta_w \mathbf{j}_w \ . \tag{21}$$

The surface current, $\mathbf{j}_w$, is computed from Ampère's law in the usual manner.

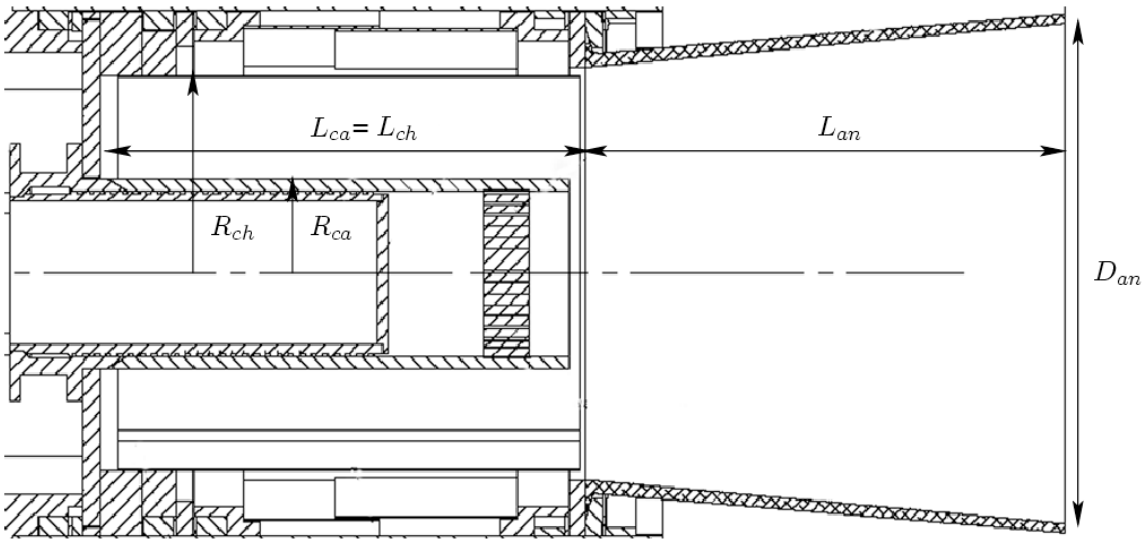

FIG. 4: Scaled engineering drawing of the Lithium Lorentz Force Accelerator (LiLFA) (from ref.[22]), where R_{ca}= 5.0 cm, R_{ch}= 11.0 cm, D_{an}= 27.0 cm, L_{ca}= 26.0 cm, L_{ch}= 26.0 cm, and L_{an}= 26.5 cm.

Freestream

The freestream region was chosen far enough down stream (22.5 cm) of the thruster exit that all the current was enclosed within the domain. Thus, from Ampère's law, the magnetic field at the free stream boundaries is zero.

Centerline

Due to symmetry, the inductive component of the electric field is zero, because there is no flow across it. However, the resistive component is finite. This can be obtained from the value of the magnetic field at a point close to $r = 0$, through a simple Taylor series expansion [27],

$$E_z|_{r=0} = E'_z|_{r=0} = \eta j_z|_{r=0} = \eta \frac{4\ B_\theta|_{\Delta r/2}}{\mu_o \Delta r}\ . \tag{22}$$

With the abovementioned boundary conditions, all the pieces are in place for the simulation of the flowfield in the LiLFA.

IV. LILFA SIMULATION RESULTS

The geometry chosen for this simulation was the LiLFA recently built at NASA-JPL[22]. The simulations reported here correspond to the nominal operational regime of the MPDT, which is defined as operation at a dimensionless current (an electromagnetic acceleration scaling parameter), ξ equal to unity. The dimensionless current ξ represents the discharge current normalized by the critical ionization current, J_{ci} at which an equi-partition of energy (or power) between the acceleration and ionization sinks is reached. At that condition, we can write[28],

$$\dot{m} u_{ex}^2/2 = T^2/2\dot{m} = \dot{m}\epsilon_i/M. \tag{23}$$

Using the Maecker thrust law[19], $T = bJ^2$, where

$$b = \frac{\mu_o}{4\pi}\left(\ln \frac{R_{an}}{R_{ca}}\right) \tag{24}$$

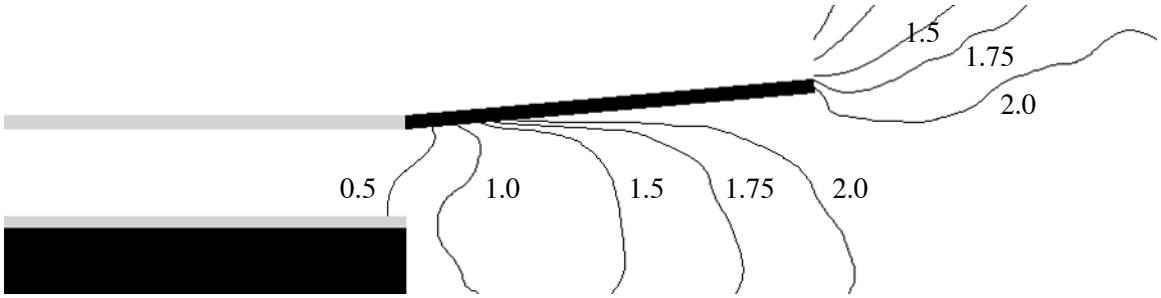

FIG. 5: Calculated Mach number contours for $\xi = 1.0$ (J = 4.5 kA and $\dot{m} = 0.25$ g/s).

is a geometrical constant, in conjunction with the so-called critical ionization velocity,

$$u_{ci} \equiv \sqrt{2\epsilon_i/M}, \tag{25}$$

and the Alfvèn critical ionization current,

$$J_{ci} = \left(\frac{\dot{m}u_{ci}}{b}\right)^{1/2}, \tag{26}$$

leads to the definition

$$\xi \equiv \frac{J}{J_{ci}}. \tag{27}$$

A number of experimental studies[28] have shown that many aspects of self-field plasma thruster performance and operation scale with ξ (or ξ^2) irrespective of power level.

We will simulate three cases that correspond to operation at nominal condition ($\xi = 1$, J = 4.5 kA, $\dot{m} = 0.25$ g/s), above that condition ($\xi = 1.34$, J = 6.0 kA, $\dot{m} = 0.25$ g/s) and below it ($\xi = 0.67$, J = 3.0 kA, $\dot{m} = 0.25$ g/s).

A. Electron Density

The electron number density contours within the thruster are shown in Fig.(9-I) for three current levels. In all cases, it can be seen that the highest density is at the inlet, as expected. The notable decrease of n_e at the anode, with increasing ξ, will be discussed in §V. As ξ increases, the plasma column in front of the inlet becomes more pronounced. This, in conjunction with the depletion of propellant near the anode, points to the increasing effect of the electromagnetic pinch with increasing current. The density in the column in front of the inlet varies from $3.5 \times 10^{20}\text{m}^{-3}$ at the inlet, to $5.0 \times 10^{19}\text{m}^{-3}$ at 15 cm downstream of the inlet, for the J = 4.5 kA (ξ=1.0) case. Radially, there is a sharp drop in density, since the expanding plasma is constricted by the pinch. At the cathode plane, the density drops sharply from $2.0 \times 10^{20}\text{m}^{-3}$ at $r = R_{ca}$ to $1.0 \times 10^{19}\text{m}^{-3}$ just 3 cm away. It is apparent that the pinch affects both the radial and the axial density distribution in the thruster.

There is also an indication in the $\xi = 0.67$ case that there is a weak shock present in the nozzle near the exit. This is seen more clearly in the velocity plots shown in Fig.(9-II).

B. Velocity

The contours of axial velocity are shown in Fig.(9-II), and the contours of Mach number for the $\xi = 1.0$ case are shown in Fig.(5). At the exit plane, velocity ranges from 16.0 to 24.0 km/s for the $\xi = 1.0$ case. The fact that the calculated value of thrust for this case is within 2% of the prediction of analytical models (see Fig.(10)) gives more credibility to the simulated values.

It is evident from the velocity plot of the $\xi = 0.67$ case (Fig.(9-II-a)) that there is a weak shock, denoted by the dotted line, which decelerates the flow in the thruster. This adverse effect only occurs for the sub-nominal condition $\xi = 0.67$. For $\xi \geq 1$, Figs.(9-II-b,c) show no such deceleration of the flow.

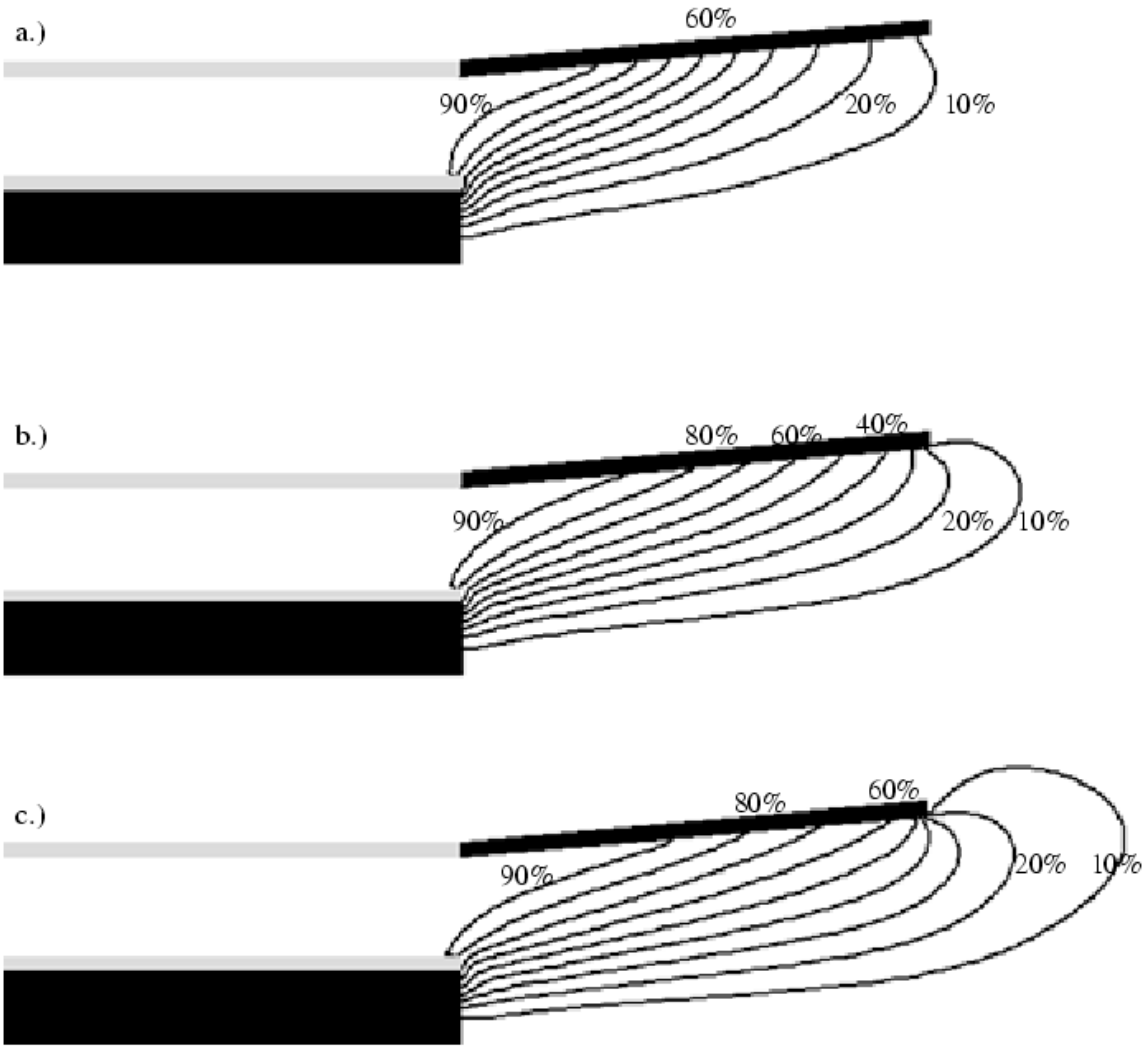

FIG. 6: Calculated enclosed current contours (% of total) for, a.) $\xi = 0.67$, b.) $\xi = 1.0$, and c.) $\xi = 1.34$.

C. Current and Potential

The calculated contours of enclosed current are shown in Fig.(6) for three different current levels. It is evident that with increasing ξ the current lines get increasing blown downstream, as has been observed in numerous MPDT experiments[29–31]. This is to be expected because as the current increases the magnetic Reynolds number grows, leading to increased downstream convection of the magnetic field.

The calculated values of the potential are shown in Fig.(7) for three values of ξ. For the nominal operating condition ($\xi = 1.0$, J = 4.5 kA, $\dot{m} = 0.25$ g/s), this simulation predicts a plasma voltage drop of 17.4 V. It is important to note that our MHD model does not include the non-quasineutral electrode sheaths, and therefore the calculated voltage corresponds to the drop across the quasineutral plasma only. Anode fall could be a significant energy sink in the MPDT, where they have been quantified experimentally. However, they have never been studied directly in the LiLFA variant. Tikhonov *et al.*[32] estimate the anode fall to be 8 V and the cathode fall to be 3 V over a wide range of operating conditions for a similar thruster, and compare these numbers to experiments. Thus, adding these estimates of electrode falls (8 + 3 = 11 V) to our calculated value of plasma drop (17.4 V at $\xi = 1.0$) results in a total voltage drop of 28.4 V. This compares favorably to the measured value of 25 V at $\xi = 1.0$. It is useful to note that the monotonic increase of voltage with current predicted by the code is consistent with measurements[1].

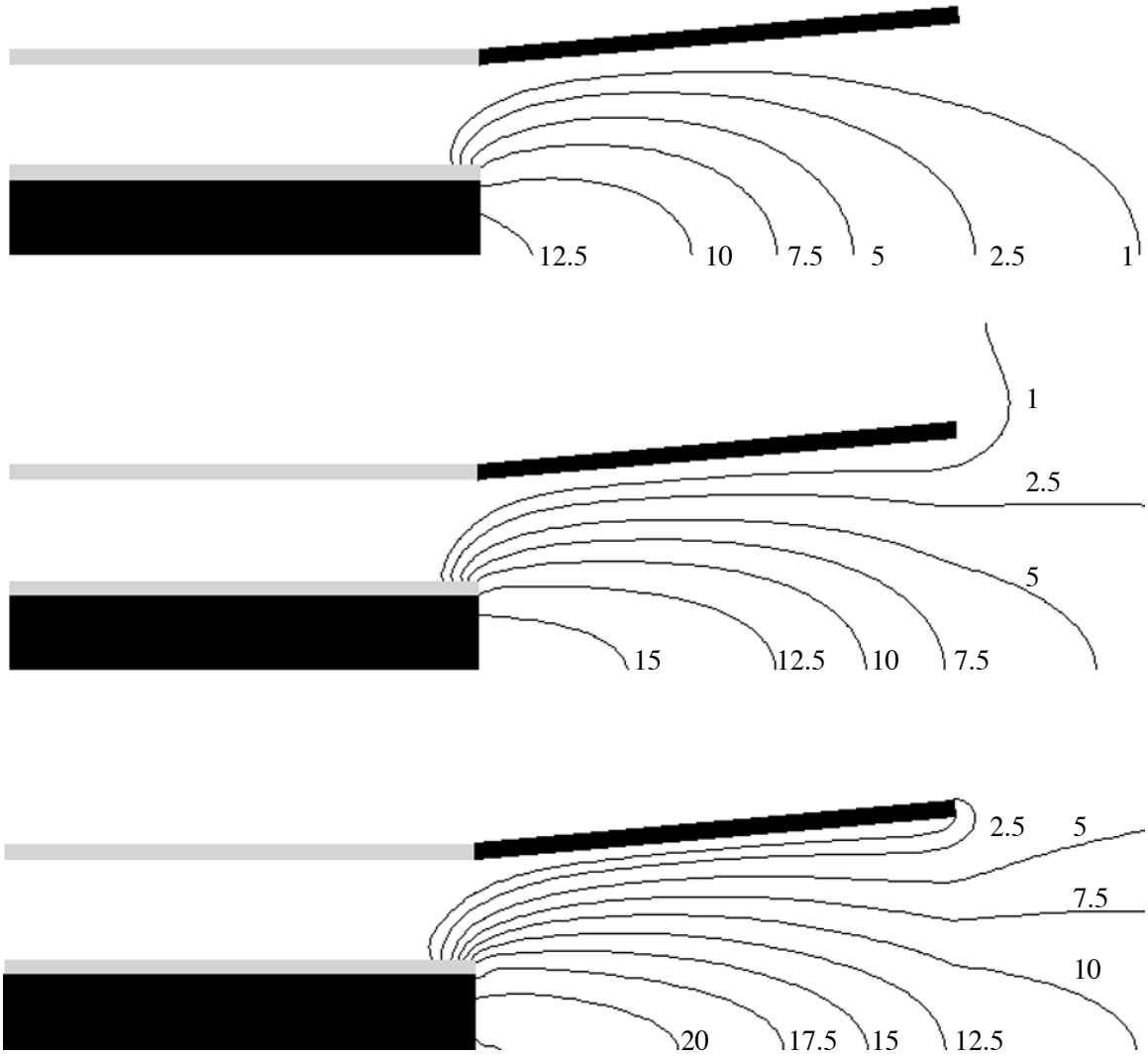

FIG. 7: Calculated potential contours (V) for, a.) $\xi = 0.67$, b.) $\xi = 1.0$, and c.) $\xi = 1.34$.

D. Electron Temperature

The calculated values of electron temperature are shown in Fig.(8) for three current levels. For the $\xi = 1.0$ case, in the bulk of the chamber, T_e ranges from 2.0 to 3.5 eV. For the ξ=1.34 case, the electron temperature reaches 7 eV. This is significantly higher than the corresponding temperature of the argon plasma in the FSBT[12]. This can be explained by the differences in the electronic structure between argon and lithium. Argon has many electronic energy levels available to absorb energy without increasing the temperature much - a fact reflected in the low value of the ratio of specific heats ($\gamma \simeq 1.15$). However, lithium does not have sufficient electronic energy levels available to absorb energy at these temperatures. Consequently, its ratio of specific heats ($\gamma \simeq 1.6$) is very close to the ideal value (5/3) at these temperatures.

It is evident from Fig.(8) that, with increasing ξ, the region of highest temperature moves upstream towards the cathode exit plane ($R_{ca} < r < R_{an}$ at $L = L_{ca}$). This is the result of high anomalous collision frequency and heating in this region, and will be discussed in the next section.

As seen in Fig.(9-I), there exists a low density plasma ($n_e \sim 10^{19}/\mathrm{m}^3$) in the non-divergent part of the channel. Since there is no current attachment and Ohmic heating, the temperature is low (≤ 0.5 eV) here. The simulation shows that the upstream flux of plasma into this region decreases with increasing ξ, and consequently the density and the temperature also decrease.

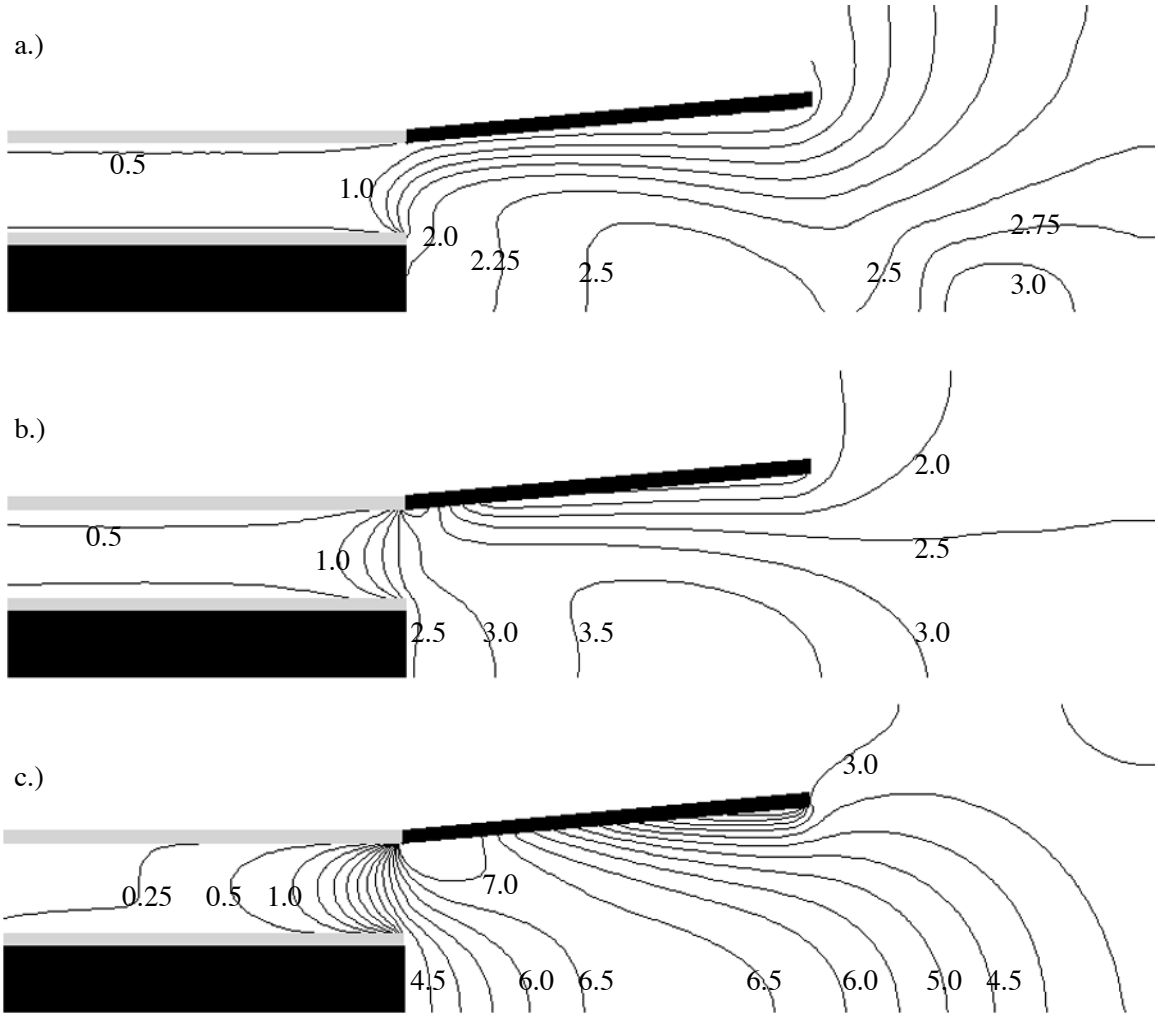

FIG. 8: Calculated electron temperature contours (eV) for, a.) $\xi = 0.67$, b.) $\xi = 1.0$, and c.) $\xi = 1.34$.

E. Anomalous Transport

Enhanced energy dissipation in plasma thrusters, due to exchange of momentum between particles and waves induced by microinstabilities, has been documented[33, 34] in gas-fed MPDTs with argon as propellant[12]. However, this effect has never been investigated in lithium plasma thrusters.

The ratio of anomalous resistivity to classical resistivity, given by eqn.(7), in the LiLFA is shown in Fig.(9-III). For the $\xi = 0.67$ case (Fig.(9-III-a)), the overall effect of anomalous transport is limited because operation at this condition is below the threshold for predominantly electromagnetic acceleration. For the higher ξ cases (Fig.(9-III-b,c)), anomalous resistivity exceeds classical resistivity at the cathode exit region and throughout the rear of the anode. This is to be expected because that is the region of highest magnetic field (Fig.(6)) and low density (Fig.(9-I)), and therefore the region of high Hall parameters that mark the escalation of anomalous transport. In the upstream and downstream regions of the anode, anomalous transport is negligible because the threshold $u_{de}/v_{ti} \geq 1.5$, where u_{de} is the electron drift velocity and v_{ti} is the ion thermal velocity, is not satisfied due to lack of sufficient current[33, 34].

As discussed earlier, the highest values of anomalous resistivity occur at the cathode exit plane, and this leads to the high temperatures observed in this region seen in Fig.(8-c).

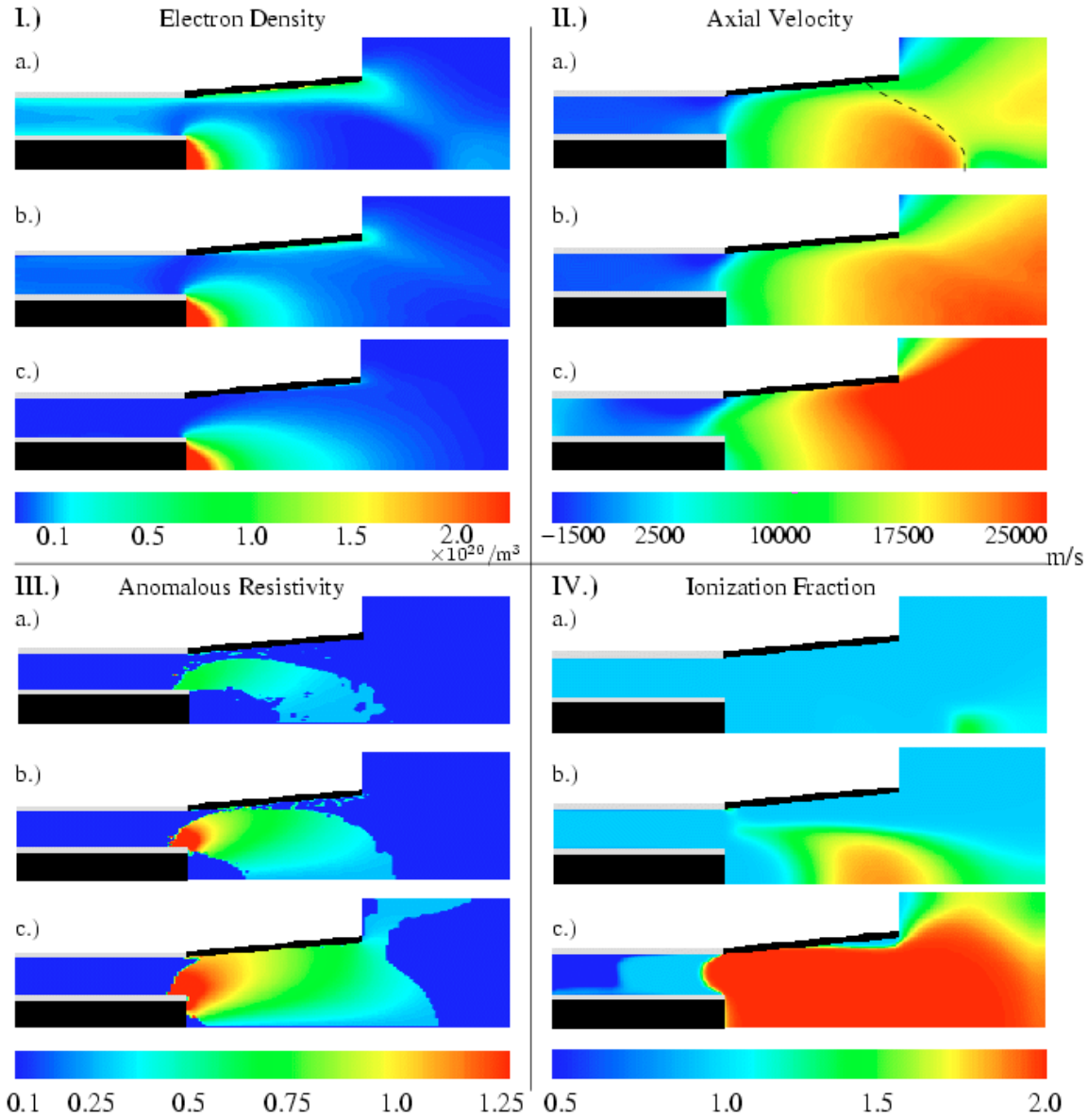

FIG. 9: Panel I shows the calculated values of electron number density (m^{-3}). Panel II shows the calculated values of axial velocity (m/s), and the dotted line in II-a indicates a weak shock. Panel III shows the calculated ratio of anomalous to classical resistivity. Panel IV shows the calculated effective ionization fraction. In each panel, the calculated values are shown for three different values of current: a.) $\xi = 0.67$, J = 3.0 kA, b.) $\xi = 1.0$, J = 4.5 kA, and c.) $\xi = 1.34$, J = 6.0 kA. The mass flow rate $\dot{m} = 0.25$ g/s in all cases.

F. Ionization

The effective ionization fraction is shown in Fig.(9-IV). It is important to bear in mind that this simulation uses an equilibrium ionization model, and hence $Z = Z(n, T_e)$ (see Fig.(2)), and therefore an understanding of T_e distribution (shown in Fig.(8)) is important to understanding the distribution of ionization levels.

Two features stand out when observing these plots: i) there is significant amount of second ionization when $\xi \geq 1$, and ii) there is a rapid change in ionization structure after ξ exceeds 1.

First, though the second ionization level of lithium is very high (75.6 eV), the equilibrium ionization model predicts doubly ionized lithium at temperatures above 5 eV. This is because the high-energy electrons at the tail, and not the bulk electrons, of the Maxwellian distribution are responsible for ionization. It is also important to note that the ionization of lithium at this temperature ($Z = 2.0$) is much less than the corresponding ionization level in thrusters

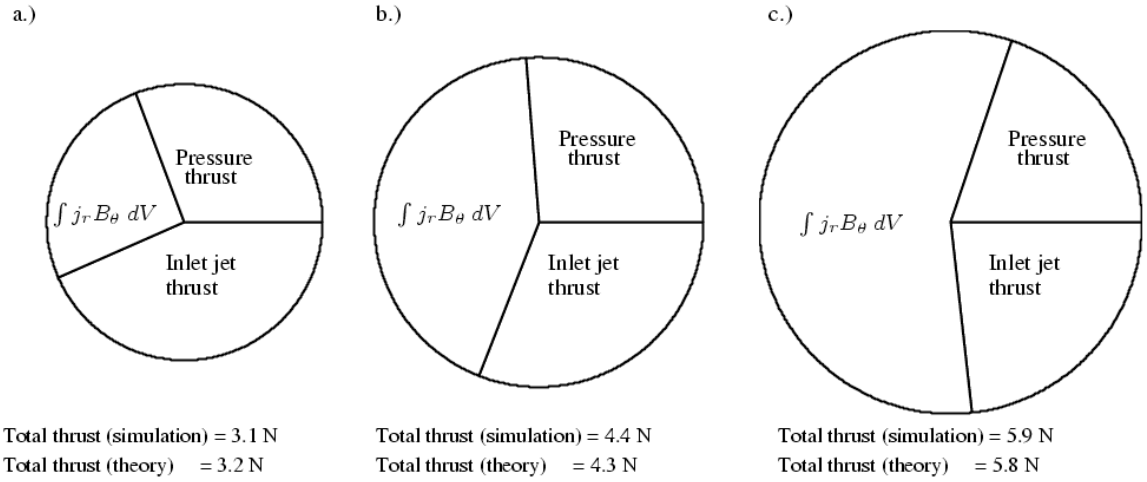

FIG. 10: Thrust components and the total thrust from the simulation are compared to the analytical value of total thrust, for a.) $\xi = 0.67$, b.) $\xi = 1.0$, and c.) $\xi = 1.34$. The part labeled $\int j_r B_\theta \, dV$ is the so-called "blowing" contribution. The relative size of each pie is in direct proportion to its total thrust.

operating with argon ($Z \simeq 5.0$)[12]. For the $\xi = 1.0$ case, the correspondence between Fig.(9-IV-b) and Fig.(8-b) is clearly seen.

Second, a notable difference in ionization structure is seen between the $\xi = 1.0$ case and the $\xi = 1.34$ case. As we mentioned earlier, the upstream plasma flux into the non-divergent part of the channel surrounding the cathode decreases with increasing ξ, consequently decreasing the temperature levels there (see the region upstream of the anode in Fig.(9-I) and Fig.(8) for increasing current levels). The equilibrium ionization model shown in Fig.(2) indicates that the ionization level changes rapidly with temperature (high $\partial Z/\partial T_e$) at $T_e \simeq 4$ eV. The 4 eV threshold is crossed in going from the $\xi = 1.0$ case to the $\xi = 1.34$ case.

V. INSIGHT INTO PHYSICAL PROCESSES

Having described the main features of the simulation results, we now turn our attention to extracting physical insight into the underlying physical mechanisms in the LiLFA. Unless explicitly stated otherwise, the focus will be on the operation at J = 4.5 kA (at $\dot{m} = 0.25$ g/s), since this corresponds to the nominal operating condition of $\xi = 1$.

A. Thrust Composition

The numerical simulation allows unique insight into the breakdown of thrust, and the scaling of its various components. The calculated values of thrust from the simulation are compared to predictions by the analytical models of Tikhonov *et al.*[32, 35], and the results are presented in Fig.(10) (the Tikhonov scaling law relies on an estimate of upstream value of the speed of sound, a_o, which is usually evaluated at a temperature between 1 eV to 2 eV).

Over a range of conditions, with $36.0 \leq J^2/\dot{m} \leq 144.0$ kA$^2/g/s$ ($0.67 \leq \xi \leq 1.34$), the code's predicted thrust agrees well with the analytical model. At $\xi \geq 1$, the agreement is within 2%. Below the nominal operating current, at $\xi = 0.67$, the code under predicts thrust by 5%, which is likely due to the existence of a velocity-reducing shock in the simulation (see Fig.(9-II-a)) that is not accounted in the analytical model.

The thrust produced by the LiLFA can be broken down into three components,

$$T = \int_{in} \rho u_z \left(\mathbf{u} \cdot d\mathbf{A}\right) + \int_V \mathbf{j} \times \mathbf{B} \; dV + \int_A p \left(\hat{z} \cdot d\mathbf{A}\right). \tag{28}$$

The first term is the thrust produced by the jet of plasma entering the thruster from the multi-channel hollow cathode. In our simulation, the entire mass flow rate of the propellant ($\dot{m} = 0.25$ g/s in this simulation) enters

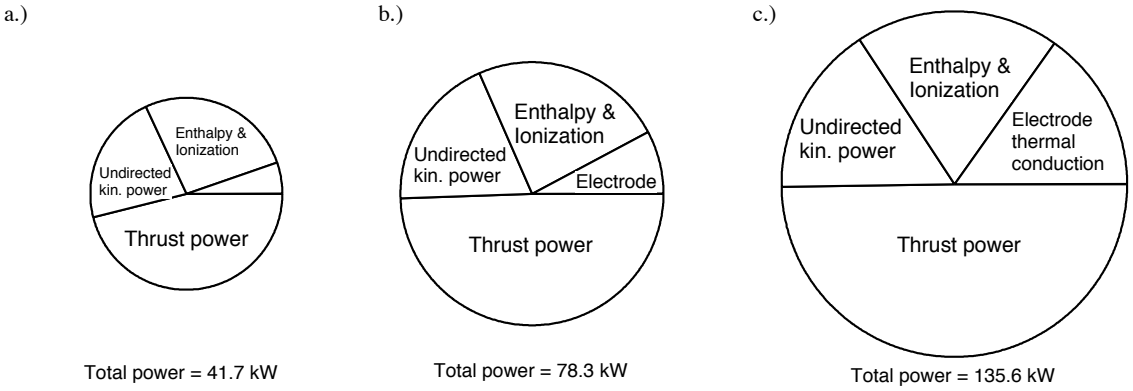

FIG. 11: Calculated power deposition fractions at, a.) $\xi = 0.67$, b.) $\xi = 1.0$, and c.) $\xi = 1.34$, with the total input power for each case given below. Power expended in radiation is $< 0.1\%$ in all three cases. The relative size of each pie is in direct proportion to its total power.

uniformly at the sonic condition, with $T_e = T_h = 0.75$ eV, and therefore the first term in eqn.(28) accounts for 1.37 N of thrust for all current levels.

The second term, the volume integral of the Lorentz body force, can be treated as the surface integral of the magnetic stress tensor[19, 28],

$$\int_V \mathbf{j} \times \mathbf{B}\ dV = \int_V \nabla \cdot \bar{\bar{\mathcal{B}}}_M\ dV = \int_S \bar{\bar{\mathcal{B}}}_M \cdot d\mathbf{S}. \tag{29}$$

Because we are interested in the axial component of force (commonly referred to as "blowing"[19]), this term has to be integrated over the inlet surface and the backplate between the cathode and the anode. The blowing contribution from the inlet surface increases from 6% at $\xi = 0.67$ to 14% at $\xi = 1.34$, while that from the backplate increases from 20% at $\xi = 0.67$ to 43% at $\xi = 1.34$. This scaling, as well as that of other components, is represented in the pie charts of Fig.(10).

The third term represents the thrust produced by gasdynamic pressure acting on the surfaces of the thruster. The radial component of the Lorentz body force contributes to thrust through unbalanced pressure distribution of the pinched gas on the surrounding surfaces. As before, this has to be integrated over the inlet surface and the backplate between the cathode and the anode. At the inlet surface, its relative contribution to total thrust decreases from 25% to 20%, though it increases in absolute magnitude. At the backplate, its relative contribution decreases from 5% at $\xi = 0.67$ to less that 0.1% at $\xi = 1.34$, and so does its absolute contribution. This is consistent with the decrease in plasma density with increasing ξ at the backplate (cf. Fig.(9-I)).

At $\xi = 1.0$, the fraction of the total thrust that is associated with electromagnetic blowing ($\int j_r B_\theta dV$) is 44%. This is noticeably smaller than the corresponding case for the Full-Scale Benchmark Thruster (FSBT), where that fraction is 75%[12], and conversely the electromagnetic pinching ($\int j_z B_\theta dV$) is less significant than in the LiLFA.

The effect of operation at $\xi \geq 1$ is a significant increase the importance of electromagnetic blowing, and a decrease in the importance of gasdynamic and pressure contributions to thrust.

B. Energy Deposition

The breakdown of various energy sinks, and their scaling with ξ, are shown in the pie charts of Fig.(11), where each pie chart shows the relative contribution of the thrust power (calculated as $T^2/2\dot{m}$), undirected kinetic power (calculated as $\int \left(\rho u^2\right) u_r dA$), enthalpy and ionization power (calculated as $\int \frac{p}{\gamma - 1}\mathbf{u} \cdot \mathbf{dA}$), and electrode thermal conduction power (calculated as $\int k \nabla T_e \cdot \mathbf{dA}$). The power lost in heating, electronic excitation, and ionization of the propellant stream amounts to 27% of the total power for the $\xi = 0.67$ case, but reduces to 20% for the $\xi = 1.34$ case. Tikhonov *et al.*[32] suggest that this number drops to 12% at higher current levels. Some of this power could possibly be recovered as directed kinetic energy. It can be observed from Fig.(11) that some 20% of the power is carried away in the form of undirected kinetic energy over the range of ξ that was considered here. The simulation also indicates that the fractional power conducted to the electrodes increases from 5% at $\xi = 0.67$ to 15% at $\xi = 1.34$.

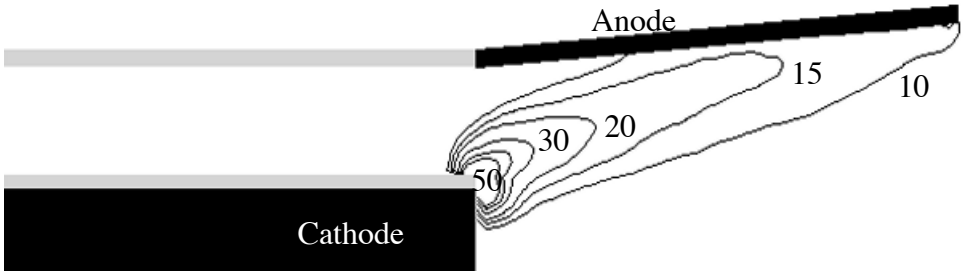

FIG. 12: Contours of constant local blowing power expenditure (in watts) at $\xi = 1.0$.

This can be attributed to the increase in temperatures, especially near the anode, over that range of ξ (see Fig.(8)). The magnitude and scaling of the actual power lost to the electrodes could well be affected by the electrode sheaths that were not included in the simulation. The fraction of the total power expended in thrust increases from 45% at $\xi = 0.67$ to 51% at $\xi = 1.34$. Since our simulation does not include electrode drops, which could be a significant energy sink, that fraction is not the same as the thrust efficiency of the device.

The above observations, especially the pie charts in Fig.(11), lead us to the following qualitative conclusions: with increasing ξ, the input power becomes approximately equipartitioned between thrust power and losses, as shown in pie chart 'c' of Fig.(11). Furthermore, the lost power itself becomes approximately equipartitioned between the three loss mechanisms, which are undirected kinetic power, enthalpy and ionization, and electrode thermal conduction.

In order to visualize the spatial distribution of the useful power (work expended by the electromagnetic blowing force), we calculate

$$P_{blow} = j_r B_\theta u_z \, dV, \tag{30}$$

and show it in Fig.(12) at $\xi = 1.0$. The figure indicates that the outer edge of the cathode is the region in which most of the work done by the electromagnetic blowing force is expended. This can be explained as follows: the magnetic field, which drops as $1/r$ between $R_{ca} < r < R_{an}$, is maximum along the outer surface of the cathode. Since the current attaches only at the cathode tip (see Fig.(6)), the product of current and magnetic field is highest in this region.

C. Anode Starvation and Current Conduction Crisis

Several experimental studies[36–38] of high-current plasma accelerators have confirmed the occurrence of performance-limiting oscillations that are onset above a particular value of current, called the "onset current" (J^*). Operation above this onset current results in notable increase in electrode ablation and a shift from a steady terminal voltage to one with high-frequency oscillations of substantial amplitude that can reach up to 100% of anode voltage. It is known[39–42] that the onset phenomenon is related to the depletion of propellant near the anode. The results of our code can be used to shed some light on this phenomenon.

Theoretically, the ratio of gasdynamic to magnetic pressure, β, equals 1 at the boundary of a pinched plasma enclosing all the mass and all the current[43] (see Fig.(13)) ($\dot{m} = \rho = p = 0$ outside). At the inlet, the current is axial and the plasma is enclosed in a free-boundary cylinder, as in the case of a classical pinch, of radius R_{ca}, and expands further downstream. Korsun[44] and Tikhonov *et al.*[32] calculate the radius of the free boundary, $R(z)$, which encloses all the propellant mass using quasi-1D ideal MHD theory ($\beta = 1$ on this boundary). Above the onset current (J^*), the pinching force causes this free boundary to move away from the anode ($R(z) < R_{an}$), preventing current conduction to the anode. This is illustrated in Fig.(14). It is believed[40–42] that this anode-starvation crisis is resolved by the discharge through a transition from diffuse arc attachment at the anode to a mode in which the current attaches in spots. These spots are believed to supply, through material evaporation, the required mass for current conduction, and their high-frequency motion is reflected as high-amplitude oscillations in the terminal voltage.

We now present, for the first time, a quantitative illustration of the role the $\beta = 1$ line plays in the anode starvation mechanism that leads to onset. It is important to note that in a real plasma pinch with finite resistivity and transport, the $\beta = 1$ line may not contain 100% of the mass. Fig.(15) shows that in our simulation, the $\beta = 1$ line coincides to the line enclosing approximately 95% of the mass, over the investigated range of ξ. This is especially the case

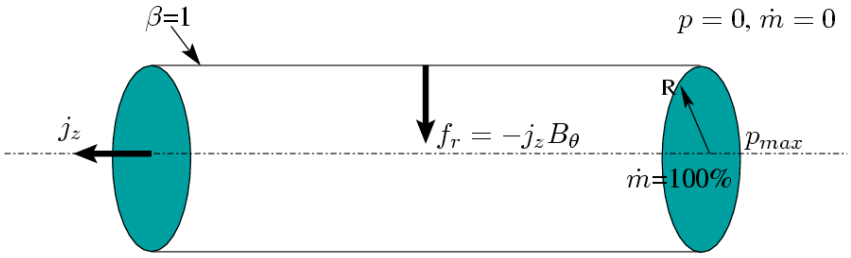

FIG. 13: Schematic of plasma constrained by magnetic pressure.

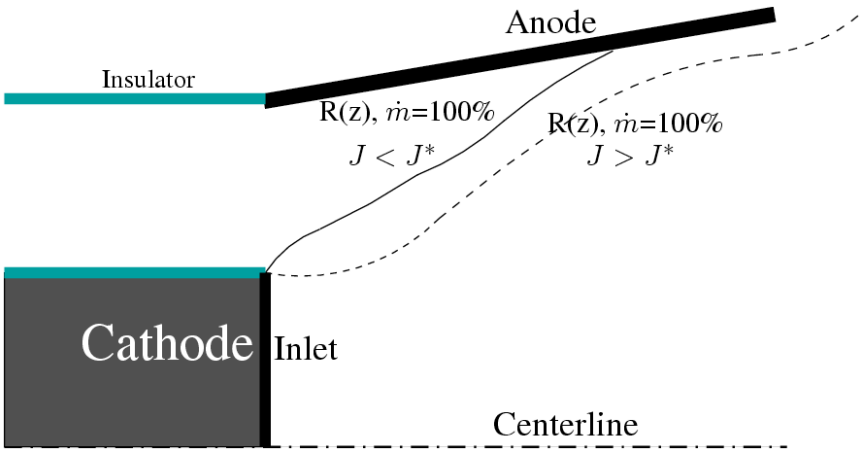

FIG. 14: Schematic of the "free boundary" (which encloses all the mass), and its variation with discharge current.

for the region immediately downstream of the cathode where the pinch is expected to occur. Therefore, Fig.(15) shows that with increasing ξ, the downstream end of the $\beta = 1$ line slides further downstream along the anode, thus leading eventually to an anode starvation crisis, as could be anticipated for operation at a value of $\xi > 1.34$ (see Fig.(15-c)). This is a clear illustration of the anode starvation mechanism and the role the $\beta = 1$ line plays in the onset phenomenon - a role that had been suspected through analytical theories of Korsun[44] and Tikhonov *et al.*[32]. Another interesting observation, obtained by comparing Fig.(15) and Fig.(6), is that only 70% of the current is enclosed by the $\beta = 1$ line, implying that some 30% of the current is conducted by only 5% of the propellant. This underscores the importance of anode starvation in the current conduction crisis reached at a high value of total current.

Fig.(16) further illustrates, more quantitatively, the relationship between the $\beta = 1$ line and anode starvation. The figure shows a plot of electron density profile along the anode at three values of ξ, with an asterisk on each curve denoting the location of the point where the $\beta = 1$ line intersects the anode. When that point meets the downstream end of the anode, as almost the case for the $\xi = 1.34$, the current conduction crisis is expected to occur. At that condition, Fig.(16) shows that the electron density has dropped a factor of five with respect to the maximum density for $\xi = 0.67$.

In the experiments by Ageyev *et al.*[1], the discharge voltage was observed to increase sharply above J = 6.5 kA at this mass flow rate. Our simulations show that at J = 6.0 kA, the β=1 line in the simulation extends to the downstream tip of the anode (see Fig.(15c)), indicating that the current will be prevented from attaching to the anode at a current not much higher than 6.0 kA. This has implications for thruster design. Since the β=1 line encompasses 95% of the propellant, it roughly delineates the free boundary of the plasma inside the LiLFA, and can be used to design an anode contour that delays onset for a given set of conditions. The design exercise, however, is beyond the scope of this paper.

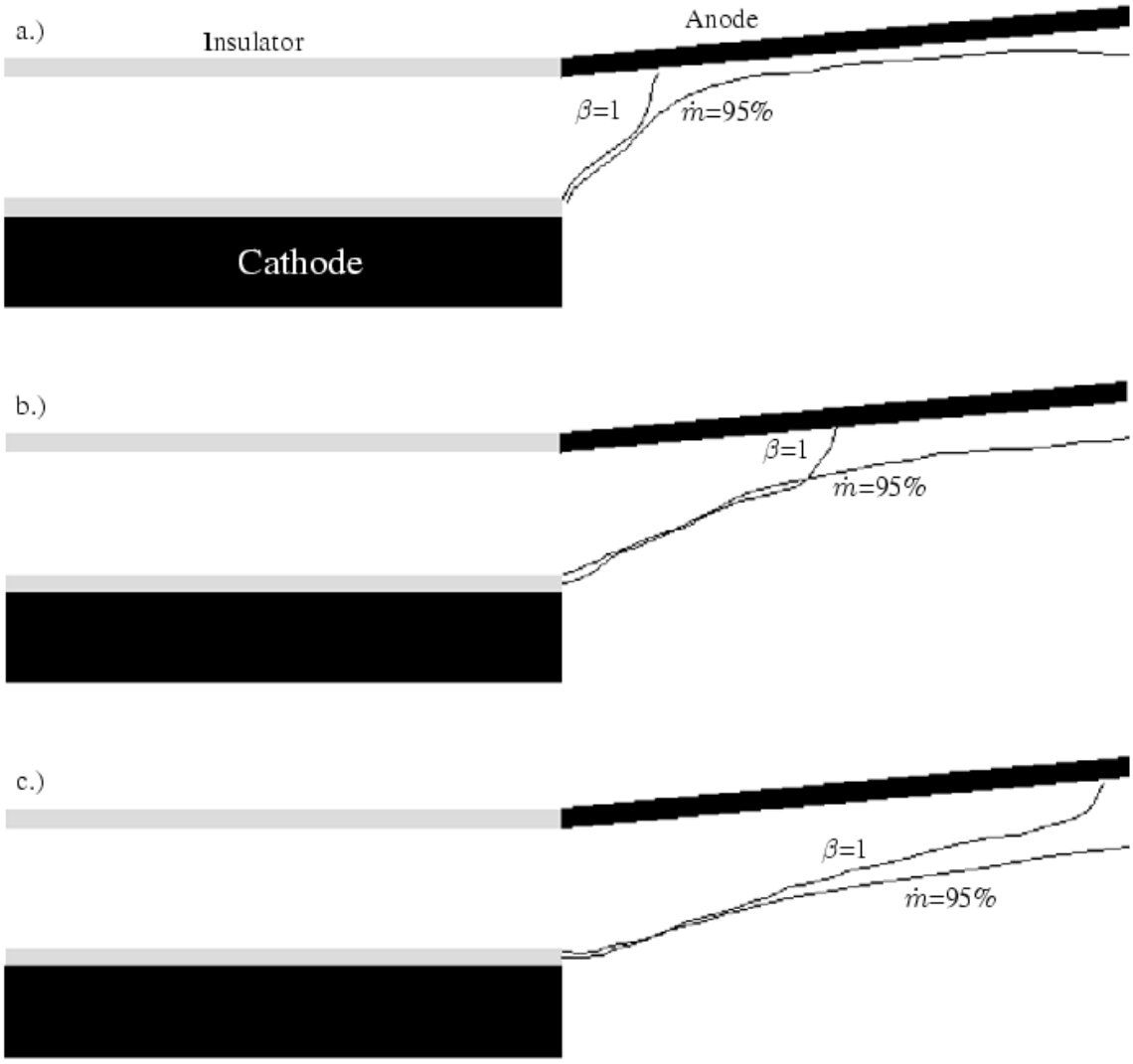

FIG. 15: Relative location of the $\beta = 1$ line to the 95% enclosed mass flux line is shown for, a.) $\xi = 0.67$, b.) $\xi = 1.0$, and c.) $\xi = 1.34$.

VI. SUMMARY

A specialized axisymmetric plasma-fluid simulation code using the state of the art numerical techniques[11] was previously validated[12] using experimental data with an argon self-field MPDT, and used here to simulate flows in the lithium Lorentz force accelerator. The goals were: i) to provide detailed flowfields inside the thruster chamber, where internal probing is extremely difficult, and, ii) to provide insight into the nature and scaling of thrust composition, energy deposition, and the onset phenomenon. In particular, the following observations and conclusions can be drawn:

- The flowfields of density, velocity, ionization, and anomalous resistivity show distinct features that have strong qualitative dependence on the total current, as it is raised through the nominal condition ($0.67 \leq \xi \leq 1.34$). In particular, for operation at a sub-nominal condition ($\xi = 0.67$), there exists a shock in the thruster that decelerates the flow. However, this detrimental structure is not present at $\xi \geq 1$.
- For operation at and above the nominal condition ($\xi = 1$) the simulations show pinching of the plasma towards the centerline, an increase in the importance of anomalous resistivity, with an associated increase in electron temperature.
- The effect of operation at $\xi \geq 1$ is a significant increase the importance of electromagnetic blowing, and a decrease in the importance of gasdynamic and pressure contributions to thrust.

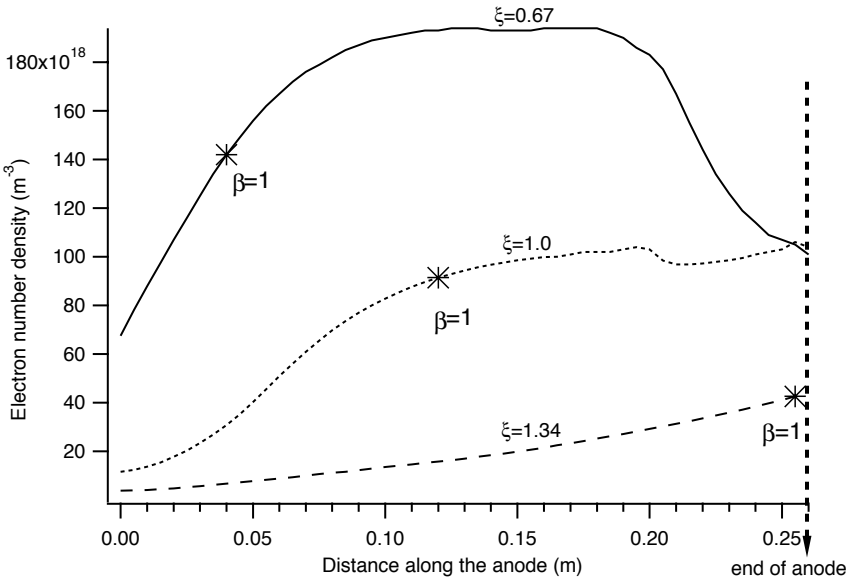

FIG. 16: Plots of calculated electron number density (m^{-3}) at the anode indicate starvation of the anode with increasing current ($\dot{m} = 0.25$ g/s in all plots). The location of $\beta = 1$ is marked on these plots to show its relevance to this starvation.

- With increasing ξ, the input power becomes approximately equipartitioned between thrust power and losses. Furthermore, the lost power itself becomes approximately equipartitioned between the three loss mechanisms, which are undirected kinetic power, enthalpy and ionization, and electrode thermal conduction.
- The $\beta = 1$ line was shown to approximately correspond to the free boundary of a classical pinch that gets exacerbated with increasing total current. The motion of this line with increasing ξ was shown to provide a clear illustration of the anode starvation mechanism that leads to the current conduction crisis called onset.

[1] V.P. Ageyev and V.G. Ostrovsky. "High-Current Stationary Plasma Accelerator of High Power". In *Proceedings of the 23rd International Electric Propulsion Conference*, Seattle, WA, USA, 1993. IEPC-93-117.

[2] S. D. Grishin, A. K. Litvak, S. N. Ogorodnikov, and V. N. Stepanov. "Intermediate-power steady-state plasma accelerator". *Sov. Phys. Tech. Phys.*, 22(2):280–285, 1977.

[3] J. E. Polk and T. J. Pivirotto. Alkali Metal Propellants for MPD Thrusters. *Conference on Advanced SEI Technologies, AIAA-91-3572*, September, 1991.

[4] V. Kim, V. Tikhonov, and S. Semenikhin. "Fourth Quarterly (Final) Report to NASA-JPL: 100-150 kW Lithium Thruster Research". *Technical Report NASW-4851*, 1997.

[5] J. E. Polk. *"Mechanisms of Cathode Erosion in Plasma Thrusters"*. PhD thesis, Princeton U., 1995.

[6] R. Frisbee and N. Hoffman. "SP-100 Nuclear Electric Propulsion for Mars Cargo Missions". In *Proceedings of the 29th Joint Propulsion Conference*, Monterey, CA, 1993. AIAA-93-2092.

[7] J. Polk, R. Frisbee, S. Krauthamer, V. Tikhonov, S. Semenikhin, and V. Kim. "Technology requirements for high-power Lithium Lorentz Force Accelerators". In *14th Symposium on Space Nuclear Power and Propulsion*, pages 1505–1513, Albuquerque, NM, 1997.

[8] K. Sankaran, L. Cassady, A. D. Kodys, and E. Y. Choueiri. A Survey of Propulsion Options for Cargo and Piloted Missions to Mars, in "Astrodynamics, Space Missions, and Chaos". *Annals of the New York Academy of Sciences*, 1017:450–467, 2004.

[9] K. Sankaran and E.Y. Choueiri. "An Accurate Characteristics-Splitting Scheme for Numerical Solution of MHD Equations". In *Proceedings of the 26th International Electric Propulsion Conference*, Kitakyushu, Japan, 1999. IEPC-99-208.

[10] K. Sankaran, E.Y. Choueiri, and S.C. Jardin. "Application of a New Numerical Solver to the Simulation of MPD Flows". In *Proceedings of the 36th Joint Propulsion Conference*, Huntsville, AL, 2000. AIAA-2000-3537.

[11] K. Sankaran, L. Martinelli, S.C. Jardin, and E.Y. Choueiri. "A Flux-Limited Numerical Method for the MHD Equations to Simulate Propulsive Plasma Flows". *Int. J. Num. Meth. Eng.*, 53(5):1415–1432, 2002.

[12] K. Sankaran, E.Y. Choueiri, and S.C. Jardin. "Comparison of Simulated Magnetoplasmadynamic Thruster Flowfields to Experimental Measurements". *Journal of Propulsion and Power*, 21:129–138, 2005.

[13] E.Y. Choueiri. "Anomalous resistivity and heating in current-driven plasma thrusters". *Phys. Plasmas*, 6(5):2290, 1999.

[14] E.Y. Choueiri. "Instability of a current-carrying finite-beta collisional plasma". *Phys. Review E*, 64(6), 2001.

[15] K. Sankaran, S.C. Jardin, and E.Y. Choueiri. "Parallelization and Validation of an MHD Code for the Simulation of Self-Field MPDT Flows". In *Proceedings of the 27th International Electric Propulsion Conference*, Pasadena, CA, 2001. IEPC-01-127.

[16] C. E. Moore. *"Atomic Energy Levels"*. National Standard Reference Data System, 1971.

[17] W. L. Wiese, M. W. Smith, and B. M. Glennon. *Atomic Transition Probabilities*. National Standard Reference Data System, 1966.

[18] M. S. DiCapua. *"Energy Deposition in Parallel-Plate Plasma Accelerators"*. PhD thesis, Princeton U., 1971.

[19] R.G. Jahn. *Physics of Electric Propulsion*. McGraw-Hill, 1968.

[20] J. Heiermann, M.Auweter-Kurtz, and P.C. Sleziona. "Adaptive Computation of the Current-Carrying Plasma in an MPD Rocket Thruster". In *Time-Dependent Magnetohydrodynamics: Anayltical, Numerical, and Application Aspects*, 1998.

[21] E. J. Sheppard. *"Ionization Nonequilibrium and Ignition in Self-Field Magnetoplasmadynamic Thrusters"*. PhD thesis, MIT, 1992.

[22] J. E. Polk. Personal communication. *NASA-JPL*, 2003.

[23] L.I. Ageyev, S.D. Grishin, V.G. Mikhalev, S.N. Ogorodnikov, and V.N. Stepanov. Characteristics of high-current plasma sources with a hollow cathode. *Radio Engineering and Electronic Physics-USSR*, 20(9):67–71, 1975.

[24] G.V. Babkin, V.G. Mikhalev, E.P. Morozov, and A.V. Potapov. An experimental investigation of a plasma in a multichannel cathode. *Journal of Applied Mechanics and Technical Physics*, 17(6):767–770, 1976.

[25] G. Popov, V. Kim, V. Tikhonov, S. Semenikhin, and M. Tibrina. "The Fourth (Final) Quarterly Report on the Milestones". *NASA-JPL-960938*, 1998.

[26] M. Krishnan, R. G. Jahn, W. F. von Jaskowsky, and K. E. Clark. "Physical Processes in Hollow Cathodes ". *AIAA Journal*, 15(9):1217–1223, 1977.

[27] K. Sankaran. "Simulation of MPD Flows Using a Flux-Limited Numerical Method for the MHD Equations". Master's thesis, Princeton University, 2001.

[28] E.Y. Choueiri. "The Scaling of Thrust in Self-Field MPD Thrusters". *J. Prop. Power*, 14(5):744–753, 1998.

[29] M. J. Boyle. *"Acceleration Processes in the Quasi-Steady Magnetoplasmadynamic Discharge"*. PhD thesis, Princeton U., 1974.

[30] D. D. Villani. *"Energy Loss Mechanisms in a Magnetoplasmadynamic Arcjet"*. PhD thesis, Princeton U., 1982.

[31] J. H. Gilland. "The Effect of Geometric Scale upon MPD Thruster Behavior". Master's thesis, Princeton University, 1988.

[32] N. V. Belan, V. P. Kim, A. I. Oranskii, and V. B. Tikhonov (Translated into English by R. Spektor). *Stationary Plasma Thrusters*. Kharkov Aviation Institute, 1989.

[33] E.Y. Choueiri, A. J. Kelly, and R.G. Jahn. Current-driven plasma acceleration versus current-driven energy dissipation: Part ii: Electromagnetic wave stability theory and experiments. *IEPC-91-100*, 1991.

[34] D.L. Tilley, E.Y. Choueiri, A. J. Kelly, and R.G. Jahn. "Microinstabilities in a 10-kilowatt Self-Field Magnetoplasmadynamic Thruster". *J.Prop.Power*, 12(2):381, 1996.

[35] V. B. Tikhonov and S. A. Semenihin. "Research on Plasma Acceleration Processes in Self-Field and Applied Magnetic Field Thrusters". In *Proceedings of the 23rd International Electric Propulsion Conference*, Seattle, WA, USA, 1993. IEPC-93-076.

[36] L. K. Rudolph. *"The MPD Thruster Onset Current Performance Limitation"*. PhD thesis, Princeton U., 1980.

[37] M. J. Wolff. "A High Performance Magnetoplasmadynamic Thruster". Master's thesis, Princeton University, 1984.

[38] J. W. Barnett. *"Operation of the MPD Thruster with Stepped Current Input"*. PhD thesis, Princeton U., 1985.

[39] F. G. Baksht, B. Ya. Moizhes, and A. B. Rybakov. "Critical mode in a coaxial plasma accelerator with external magnetic field". *Soviet Physics Technical Physics*, 21(2):150–152, 1976.

[40] A.D. Gallimore, A.J. Kelly, and R.G. Jahn. "Anode Power Deposition in Magnetoplasmadynamic Thrusters". *J. Propulsion & Power*, 9(3):361–368, 1993.

[41] E. H. Niewood. *"An Explanation for Anode Voltage Drops in an MPD"*. PhD thesis, MIT, 1993.

[42] Kevin D. Diamant, Edgar Choueiri, and R.G. Jahn. "The role of spot mode transition in the anode fall of pulsed MPD thrusters". *J. Propulsion & Power*, 14(6):1036–1042, 1998.

[43] R. J. Goldston and P. H. Rutherford. *Introduction to Plasma Physics*. Institute of Physics Publishing, 1995.

[44] A. G. Korsun. "Current limiting by self magnetic field in a plasma thruster". *Soviet Physics Technical Physics*, 19:124–126, 1974.